Supporting Information

for

Multi-State Multi-Configuration Quantum Chemical Computation of the Two-Photon Absorption Spectra of Bovine Rhodopsin

Samira Gholami[a], Laura Pedraza-González[b], Xuchun Yang[a], Alexander. A. Granovsky[c], N. Ilya., Ioffd[c] Massimo Olivucci[a,b*]*

[a]Department of Chemistry, Bowling Green State University, Bowling Green, Ohio 43403, United States

[b]Department of Biotechnology, Chemistry and Pharmacy, Università di Siena, via A. Moro 2, I-53100 Siena, Siena, Italy

[c]Firefly Project, Moscow 117593, Russia

[d]Department of Chemistry, Lomonosov Moscow State University, 119991 Moscow, Russia

Table of contents:

S1. Computational Methods

This section outlines the methods and strategies used to calculate the TPA spectra of Rh. In subsection ***S1.1***, we explain how we constructed the QM/MM model of Rh. The procedure to calculate the OPA and TPA spectroscopic parameters is then presented in subsection ***S1.2***. Finally, in subsection ***S1.3*** we explain how the TPA spectra is simulated by applying the Sum-Over-State (SOS) approximation.

S1.1 Construction of the QM/MM model

The QM/MM model of Rh was constructed using the a-ARM version[1] of the Automatic Rhodopsin Modeling (ARM) protocol,[2] whose flowchart is shown in **Figure S1**. The protocol, for now on simply called a-ARM, is not designed to produce the most accurate QM/MM model possible but basic, computationally fast monomeric gas-phase models with electrostatic embedding aimed to the rationalization or prediction of spectroscopic and photochemical property trends. *a*-ARM only requires a PDB ID, or a template PDB file, to generate an input file in PDB format which contains information on the protein structure, including rPSB11 and excluding membrane lipids and ions, with the assigned protonation states of all residues that can be ionized and, finally, the positions of Na^+/Cl^- counter-ions needed to neutralize both intracellular (IS) and extracellular (OS) protein surfaces (see **Figure S2**). An additional input file containing the list of residues constituting the hosting chromophore cavity is also generated (see **Figure S1A**). As shown in **Figure S2**, the final model is characterized by the environment, cavity and Lys-QM subsystems. The first two subsystems and the Lys-296 residue atoms (excluding the terminal NH_2-Cε moiety) form the MM part of the model while the QM part is formed by the rPSB11 chromophore plus the Cε atom of the Lys-296 side chain. Accordingly, the Lys-QM subsystem contains both MM and QM atoms as well as the frontier between the MM and QM parts. A hydrogen link atom inserted at the truncated Cε−Cδ bond and covalently linked to the Cε atom of the QM subsystem saturates the valence bond between the QM and MM atoms along the Lys-296 side chain. Therefore, QM part contained 54 atoms. Suitably modified point charges and parameters have been used for the MM part of the Lys-296 residue linked to the chromophore.[3-4]

The Rh model was generated starting from the protein X-ray crystallographic (PDB ID 1U19[5]), by using the *a*-$ARM_{default}$ approach with the following default parameters: chain A; list of the residues defining the chromophore cavity computed via Voronoi tessellation and alpha spheres theory, and

including the Lys-296 residue covalently linked to the rPSB11 chromophore, plus the Glu-113 main (MC) and Glu-181 secondary (SC) counter-ion residues; neutral form of the residues Asp-83, Glu-122, Glu-181, His-211 (δ-nitrogen of the imidazole protonated), based on partial charges calculated at the crystallographic pH 6.0; and the inclusion of 2 Na^+ and 6 Cl^- counter-ions, with positions optimized with respect to an electrostatic potential grid constructed around each charged OS or IS target residue. Crystallographic water molecules are optimized using DOWSER.[6]

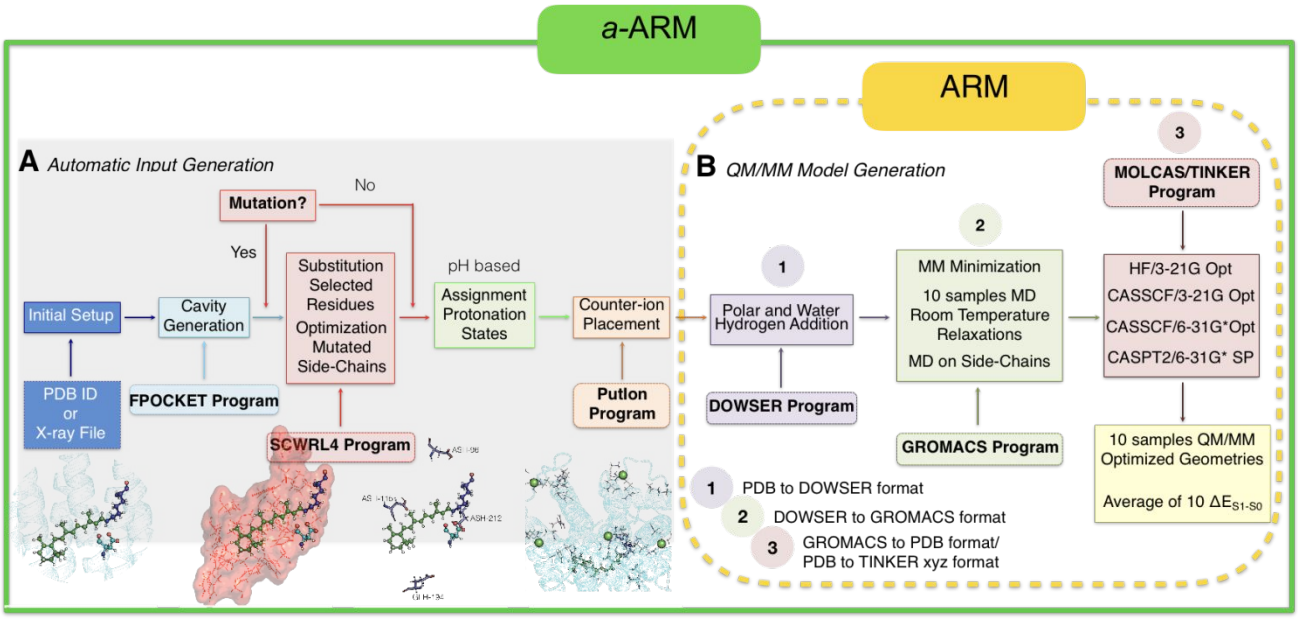

Figure S1. *General workflow of the a-ARM protocol used for the generation of the QM/MM models of Bovine Rhodopsin.*

In order to obtain a better prediction of the spectra, *a*-ARM constructs 10 independent replicas of the Rh QM/MM model (model-1 to model-10), by starting with 10 different independent sets of initial velocities the simulated annealing/molecular dynamics step in Figure S1 performed by GROMACS[7]. This is followed by QM/MM geometry optimization relaxing both the Lys-QM and cavity subsystems optimization at the CASSCF/AMBER levels, using a combination of MOLCAS[8] and TINKER[9]. The TINKER[9] software package was coupled to MOLCAS to perform the QM/MM calculations using the AMBER-FF94[10] parameters. The description of the electrostatic embedding of the QM subsystem into the MM subsystem was treated using the electrostatic potential fitted methodology.[11-14]

The performance of the Rh QM/MM models was evaluated by comparing the average vertical excitation energies $\langle \Delta E_{S1-S0} \rangle$ calculated at CASPT2//CASSCF/6-31G(d)/AMBER level of theory (*i.e.* the QM/MM model structures were optimized at the single-root CASSCF/6-31G(d) level) with the experimental value, 57.4 kcal/mol (this is obtained by converting the 498 nm photon wavelength corresponding to the absorption maxima in energy). The results, reported in **Table S1**, showed that the average computed ΔE_{S1-S0} value is 57.3±0.5 kcal/mol (λ_{max} = 499±4 nm), that differs from the experiment for less than 1 kcal/mol. As described in the next section the final energies of the constructed QM/MM model is computed at the XMCQDPT2/cc-pVTZ level of theory yielding a model which can be labelled as XMCQDPT2/cc-pVTZ//CASSCF/6-31G(d)/AMBER level.

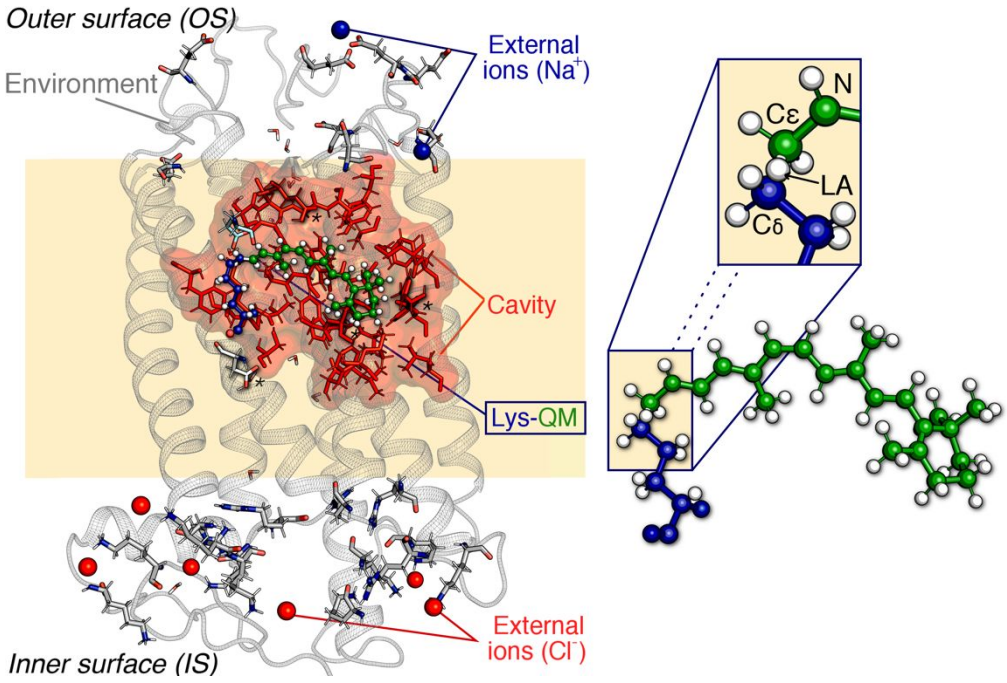

Figure S2. *General scheme of Rh QM/MM model generated by a-ARM. This is composed by: (left) environment subsystem (gray cartoon), chromophore rPSB11 (green ball-and-sticks), Lys-296 side-chain covalently linked to the rPSB11 chromophore (blue ball-and-sticks), main counter-ion Glu-113 MC (cyan tubes), residues of the chromophore cavity subsystem (red tubes), protonated residues Ash-83, Glh-122, Glh-181, Hid-211 (tubes marked with *), and external Cl^- (red balls) and Na^+ (blue balls) counter-ions. Right: The rPSB11 chromophore (green) and the linked Lys-296 side chain fragment (blue) form the Lys-QM subsystem which includes the H-link atom located along Cε−Cδ connecting blue and green atoms*

(please see the inset) which belong to the MM and QM parts of the model. The H-link atom has been indicated with "LA" in the inset.

Table. S1. *Vertical excitation energies ($\Delta E_{S1\text{-}S0}$, kcal/mol) and maximum absorption wavelengths (λ_{max}, nm), and oscillator strength (f_{Osc}) of the Rh models calculated at the CASPT2/6-31G(d)//CASSCF/6-31G(d)/AMBER level of theory. Differences between calculated and experimental data ($\Delta\Delta E^{exp}_{S1\text{-}S0}$, $\Delta\lambda^{Exp}_{max}$) are also presented.*

Structure (seed)	**$\Delta E_{S1\text{-}S0}$ (kcal/mol)**	**λ_{max} (nm)**	***f* Osc**	**$\Delta\Delta E^{Exp}_{S1\text{-}S0}$ (kcal/mol)**	**$\Delta\lambda^{Exp}_{max}$, (nm)**
model 1 (01837)	58.0	493	0.86	0.6	-4.7
model 2 (18273)	57.6	496	0.86	0.2	-1.7
model 3 (28374)	56.9	502	0.85	-0.5	4.4
model 4 (3824)	57.0	501	0.87	-0.4	3.2
model 5 (4567)	56.8	503	0.90	-0.6	5.1
model 6 (55555)	57.5	497	0.87	0.1	-1.0
model 7 (666)	57.0	502	0.90	-0.4	3.8
model 8 (7834)	56.7	504	0.87	-0.7	5.9
model 9 (87654)	57.0	502	0.90	-0.4	3.6
model 10 (999)	58.0	493	0.92	0.6	-4.8
Average	**57.3**	**499**	**0.88**		
DESV.ST	**0.5**	**4**			
Exp	**57.4**	**498**			

S1.2 Calculation of the spectroscopic parameters

The QM/MM model-1 to model-10 replicas are used for the simulation and characterization of the OPA and TPA spectroscopic parameters. This task was carried out using the Firefly quantum chemistry package version 8.2.0 partly based on the GAMESS(US)[15] source code. The wavelength of the OPA maxima (λ_{max}) of each model, more specifically, corresponding vertical excitation energies at the Franck-Condon (FC) points, dipole moments and transition dipole moments were

computed by means of the extended multiconfigurational quasi-degenerate perturbation theory XMCQDPT2,[16] which has been shown to yield accurate excitation energies in complex fluorophores.[17] XMCQDPT2 was applied on top of the CASSCF/cc-pVTZ computation with (12e,12o) active space that encompassed the whole π-system of rPSB11. The Intruder State Avoidance (ISA) parameter was set to 0.02 Hartree.[17] To speed up the calculations, the Resolution of Identity (RI) approximation was employed. The RI approximation (also known as Density Fitting or DF) aims to reduce the cost of computations using an auxiliary (*i.e.* fitting) basis set. The auxiliary basis sets are not implemented in Firefly but obtained from an external library file (http://classic.chem.msu.su/gran/gamess/).

To obtain reliable results, both the XMCQDPT2/CASSCF state-averaging scheme and the size of the XMCQDPT2 model Hamiltonian are of critical importance. Inclusion of higher-energy CASSCF roots into the model Hamiltonian, though costly, generally improves the description of the target low energy states of interest.[16] In addition, incorporation of higher-energy roots partially de-contracts the model reference CASCI vectors thus allowing more flexibility in the description of the target states.[18] On the contrary, broader state averaging in the CASSCF procedure typically worsens the description of each individual state entering the state-averaging.[18] Therefore, only those CASSCF roots that gave important contributions to the zero-order part of the XMCQDPT2 wave-function of our target states, *i.e.* S_0, S_1, S_2 and S_3, were included in the averaging. Looking at the eigenvectors of the model Hamiltonian of the XMCQDPT2 single point calculation shows that the target states are covered by the first eight CASSCF roots (generally above 0.1 by weight). Thus, for the Rh model including the rPSB11 chromophore, single point calculations were safely performed with the averaging over the eight lowest CASSCF roots (hereafter SA8) and, based on previous computations on conjugated chromophores of similar size,[18] 12-root in the XMCQDPT2 model Hamiltonian.

For further validation of the accuracy and applicability of the XMCQDPT2 method, we computed OPA properties (transition energies and oscillator strengths) of the QM/MM model of Rh with the XMCQDPT2//CASSCF and CASPT2//CASSCF levels of theory and compared the results with the experimental values. For this aim, we selected model-6, as the representative Rh structure, featuring the CASPT2//CASSCF/6-31G(d) transition energy $\Delta E_{S1\text{-}S0}$ (λ_{max}) closest to the 10 models average $\Delta E_{S1\text{-}S0}$ value (**Table S1**). All CASPT2 calculations were carried out with the IPEA parameter set to zero using the MOLCAS code.[8]

The gas-phase *trans*-stilbene and its acceptor–π–donor (A–π–D) derivative 4-dimethylamino-4'-nitrostilbene (hereafter referred to as ACCD) chromophores were used as benchmarks to validate the protocol for TPA spectra simulation. We selected ACCD because it features a non-centrosymmetric π-conjugation similar to rPSB11. To do so, we employed, for *trans*-stilbene, the 12-root SA6-XMCQDPT2 calculation with a complete π-orbital (14e,14o) active space and the cc-pVTZ basis set benchmarked and employed in a previous study,[18] using the C_2 symmetric CASSCF/6-31G(d) ground state geometry. In the case of ACCD, a complete active space of 20 electrons in 18 orbitals, comprising all π and n orbitals which contribute to the conjugation, is too large to handle and, consequently, prevented us to perform the geometry optimization at that level. On the other hand, we noticed that the CASSCF/6-31G(d) optimized geometry of *trans*-stilbene is very close to the previously reported MP2/cc-pVTZ geometry.[18] Furthermore, as shown in the **Section S6**, the TPA spectra of the *trans*-stilbene is not intensely affected by differences in the geometry. Accordingly, the geometry of ACCD is optimized at MP2/cc-pVTZ level of theory. Identical to the *trans*-stilbene, a 12-root SA6-XMCQDPT2 calculation with a (14e,14o) active space is employed to obtain the TPA properties of ACCD as, to further decrease the computational cost and as a further approximation, the lone pair electrons of dimethyamino and π/n electrons of nitro substitutes are excluded from the active space.

S1.3 Calculation of the TPA cross section

TPA is a third-order nonlinear optical process, first predicted by Göppert-Mayer in 1931[19] and observed by Kaiser and Garrett in 1961.[20] These phenomena involve electronic excitation of a molecule by a simultaneous absorption of a pair of photons of the same or different energies and therefore λ_{max}. TPA is now of interest for new technologies in various areas such as three dimensional fluorescence microscopy,[21-22] up conversion lasing,[23-24] optical power limiting,[25-26] photodynamic therapy,[21] three dimensional microfabrication,[27-28] optical data storage,[29-31] and two-photon optogenetics,[32] –where the IR activation of genetically encodable actuators, silencer and reporter based on microbial rhodopsins is highly desirable [33-35]– more specifically, using Channelrhodopsin-2 (ChR2).[32, 34-41] Compared with the visible light employed in one-photon absorption (OPA), IR light has higher penetration depth and lower scattering in human tissues prompting the search for chromophores with large TPA cross-section. However, the search for new and more effective TPA molecules or, in the case of proteins, mutants is limited and the possibility

to design new molecules with all the desirable TPA properties (maximum absorption wavelength, $\lambda_{max,\ TPA}$ and cross-section, σ_{TPA}) is still an open question.[42-44] Due to these difficulties, a number of attempts to establish a computational protocol for the simulation of the TPA properties of chromophores possessing large cross sections, have been reported.[45-52] These protocols provide an attractive alternative to systematic time consuming synthesis and necessary nonlinear optical measurements.

Precise experimental and theoretical evaluation of the absolute σ_{TPA}, which determines the intensity of the TPA transition, is a demanding task requiring independent experimental evaluation of several parameters, each of which has a specific error that contributes to the uncertainty in the observed or computed value. For example, the diverse σ_{TPA} peaks reported for the Enhanced Green Fluorescent Protein (EGFP) range from 1.5 to 300 GM and are attributed to different sources of errors.[53] Computationally, the evaluation of the transition dipole moments between ground and excited states, excited state energies, sensitivity to the environment and the value of the pre-factors necessary to convert the microscopic TPA strength (*i.e.* δ_{TPA}) to the macroscopic cross-section (*i.e.* σ_{TPA}), challenge the accurate prediction of σ_{TPA} values and their comparison with experimental data. In recent years, a number of benchmarking studies on σ_{TPA} calculations have appeared in the literature[46, 48, 51, 54-55]. For instance, *K. D. Nanda et.al*[55] presented a formalism for the computation of σ_{TPA} of some model chromophores based on an equation-of-motion excitation energy coupled cluster single and double (EOM-EE-CCSD) wave functions showing the robustness of the method. They also concluded that the CC2 method strongly overestimates the σ_{TPA} value when compared to the result of higher-level EOM-CCSD calculations. After that, *Beerepoot et al.* showed that δ_{TPA} values computed with the CC2 method are only slightly overestimated compared to the EOM-EE-CCSD and that the reported overestimated σ_{TPA} values are a result of inconsistencies in the conversion of the δ_{TPA} to σ_{TPA} values. On the other hand, the fact that δ_{TPA} values computed at the TD-DFT/CAM-B3LYP level of theory are found to be 1.5 to 3 times smaller than the coupled-cluster reference has been linked to an underestimation of excited-state dipole moments.[46] EOM-EE-CCSD has been also used to calculate the OPA and TPA properties of *trans*- and *cis*-stilbene.[52] The described discrepancies show the importance of the quantum chemical method employed in calculating the necessary excited state properties: dipole and transition dipole moments and transition energies (*i.e.* vertical excitation energies).

TPA can occur when the electron of a molecule is excited from ground state to excited state (final state) by the simultaneous absorption of two photons via an intermediate state.[56-58] Such a nonlinear process is related to the second hyperpolarizability [50] of the molecule. Many studies have been done to quantify the two-photon absorption and calculate the σ_{TPA} so far. [46, 48-49, 55] *Fortrie et al.* [49] have established an approach to quantify the two-photon absorption. For that purpose, they defined a way of computing σ_{TPA} which, for TPA, has the same significance of the oscillator strength of OPA.
The TPA cross section is related to the imaginary part of the second hyperpolarizability. Here, the following equations (equations "F1" and "D2" in the *Fortrie et al.* contribution [49]), have been used to calculate the TPA line-shape as a function of the frequency ω (*i.e.* the excitation wavelength):

$$\sigma_{TPA}(\omega) = \frac{\mu_0 \hbar \omega^2}{\varepsilon_0 [n_s(\omega)]^2}\left(\frac{[n_s(\omega)]^2 + 2}{3}\right)^4 \times \mathrm{Im}$$
$$\left[\frac{1}{15}\sum_{i,j}\gamma_{iijj}(-\omega;-\omega,\omega,\omega) + \gamma_{ijij}(-\omega;-\omega,\omega,\omega) + \gamma_{ijji}(-\omega;-\omega,\omega,\omega)\right] \quad (1)$$

Here, n_s is the refractive index, μ_0 is the vacuum susceptibility, ε_0 is the vacuum permittivity and γ represents the second hyperpolarizability where the sum is over the Cartesian components. The hyperpolarizability can be expressed through the components of the dipole operator, transition frequencies and state widths (for additional details see reference 44). A molecular system is characterized by its electronic m eigenstates with E_m energies and the half-life times τ_m. By considering a power expansion of the energy with respect to the applied field, the sum-over-state (SOS) expression used to evaluate the Cartesian components of the γ is given by: [49-50, 59]

$$\gamma_{ijkl}(-\omega_\sigma;-\omega_1,\omega_2,\omega_3)=\frac{3}{2\hbar^3}I^{j,k,l}_{\omega_1,\omega_2,\omega_3}\sum_{m\neq q}\sum_{p\neq q}\Bigg\{\sum_{n\neq q}\Bigg[\frac{\langle q|\mu_i|m\rangle\langle m|\bar{\mu}_j|n\rangle\langle n|\bar{\mu}_k|p\rangle\langle p|\mu_l|q\rangle}{(\Omega_{qm}-\omega_\sigma)(\Omega_{qn}-\omega_1-\omega_2)(\Omega_{qp}-\omega_1)}$$
$$+\frac{\langle q|\mu_j|m\rangle\langle m|\bar{\mu}_i|n\rangle\langle n|\bar{\mu}_k|p\rangle\langle p|\mu_l|q\rangle}{(\Omega^*_{qm}-\omega_3)(\Omega_{qn}-\omega_1-\omega_2)(\Omega_{qp}-\omega_1)}+\frac{\langle q|\mu_l|m\rangle\langle m|\bar{\mu}_k|n\rangle\langle n|\bar{\mu}_i|p\rangle\langle p|\mu_j|q\rangle}{(\Omega^*_{qm}+\omega_1)(\Omega^*_{qn}+\omega_1+\omega_2)(\Omega_{qp}-\omega_3)}$$
$$+\frac{\langle q|\mu_l|m\rangle\langle m|\bar{\mu}_k|n\rangle\langle n|\bar{\mu}_j|p\rangle\langle p|\mu_i|q\rangle}{(\Omega^*_{qm}+\omega_1)(\Omega^*_{qn}+\omega_1+\omega_2)(\Omega_{qp}-\omega_\sigma)}\Bigg]-\frac{\langle q|\mu_i|m\rangle\langle m|\mu_j|q\rangle\langle q|\mu_k|p\rangle\langle p|\mu_l|q\rangle}{(\Omega_{qm}-\omega_\sigma)(\Omega_{qm}-\omega_3)(\Omega_{qp}-\omega_1)}$$
$$-\frac{\langle q|\mu_j|m\rangle\langle m|\mu_i|q\rangle\langle q|\mu_k|p\rangle\langle p|\mu_l|q\rangle}{(\Omega_{qm}-\omega_3)(\Omega^*_{qp}+\omega_2)(\Omega_{qp}-\omega_1)}-\frac{\langle q|\mu_j|m\rangle\langle m|\mu_i|q\rangle\langle q|\mu_l|p\rangle\langle p|\mu_k|q\rangle}{(\Omega^*_{qm}+\omega_\sigma)(\Omega^*_{qm}+\omega_3)(\Omega^*_{qp}+\omega_1)}$$
$$-\frac{\langle q|\mu_j|m\rangle\langle m|\mu_i|q\rangle\langle q|\mu_l|p\rangle\langle p|\mu_k|q\rangle}{(\Omega^*_{qm}+\omega_3)(\Omega_{qp}-\omega_2)(\Omega^*_{qp}+\omega_1)}\Bigg\}$$

(2)

Where $I^{j,k,l}_{\omega_1,\omega_2,\omega_3}$ represents the average operator over all simultaneous permutations of indexes and exponents, $\omega_\sigma=\omega_1+\omega_2+\omega_3$ is the polarization response frequency. ω_1, ω_2 and ω_3 indicate the frequencies of the perturbing radiation fields (in the degenerate case considered here, TPA, $\omega_1=\omega_2=\omega$ and $\omega_3=-\omega$), *i, j, k* and *l* correspond to the molecular axes *x*, *y* and *z*; *m*, *n* and *p* denote excited states and *q*, the ground state. μ_j is the *j*(x, y, z)th component of the dipole operator and $\langle m|\bar{\mu}_j|n\rangle=\langle m|\mu_j|n\rangle-\langle q|\mu_j|q\rangle$. In this equation, $\Omega_{mn}=\omega_{mn}-i\Gamma_{mn}/2$, $\Gamma_{mn}=\Gamma_n-\Gamma_m$, Γ_m is equal to $2\pi/\tau_m$, and $\omega_{mn}=\frac{(E_n-E_m)}{\hbar}$. Γ_{mn} (also known as the damping factor) has been set to 0.2 eV (as the full width at half maximum (FWHM)) in all cases. Since any reliable theoretical estimate of the damping factor is hardly possible, hence, the choice of damping factor value could be based on either the empirical fitting to the experimental widths or using the standard value. Here, we selected 0.2 eV following the standard conventions in the field of TPA simulations and also based on the fitted experimental values.[52]

Normally, the appreciable contributions to σ_{TPA} are due to the intermediate states that are located close to the final state and, preferably, lower. Therefore, TPA calculations for the lowest excited states require a limited number of intermediate states to be included in the sum. As explained above, our multi-state level considered eleven XMCQDPT2 excited states for Rh, *trans*-stilbene and ACCD. The calculations produced the relevant transition energies corrected at the second order and the dipole and transition dipole moments based on the zero-order XMCQDPT2 density. Using such set of input, γ and the TPA line-shape were calculated according to the equations (2) and (1), respectively, by means of a Fortran code written by one of the authors.

S1.4 Semi-classical trajectory calculations

Franck-Condon (FC) trajectories are semi-classical (*i.e.* non-adiabatic) trajectory starting at the equilibrium structure of the QM/MM model described above with zero initial velocities. The ultrafast lifetime of the Rh photoisomerization ensure that these trajectories describe the average evolution of the corresponding excited state population. Since we are only interested in the evolution from the FC point to the decay to S_0 (*i.e.* most probably in the region of a S_1/S_0 conical intersection), all trajectories were propagated according to a deterministic surface-hop method implemented in the MOLCAS module Dynamix (see reference[60] for details) for a 200 fs time threshold and an integration step of 1 fs. Notice that this is a modified version of widely used Tully[61] method where the random number is fixed at a certain value (0.25). [62]

The exact protocol employed for FC trajectory calculation depends on the initial excited state. For the S_1 the calculations were performed with two-root state-average while three-root state-average CASSCF/6-31G(d)/AMBER level applied for S_2 and S_3 states (the upper three roots when S_3 is the initial state). However, after the decay to S_1, the trajectory calculations were interrupted and continued using two-root, rather than three-root, state-averaged calculations as the best compromise for the quality of the S_1 CASSCF wave function. In fact, while a charge-transfer character dominates the S_1 state, the third and fourth roots (S_2 and S_3) have covalent (diradical) character (see section ***S2***) leading to a far too high covalent character of the S_1 state upon state averaging [62-63]. This leads to a S_1 gradient (*i.e.* slope of the S_1 potential energy surface), which is significantly lower than the correct one as the system progress towards the S_1 to S_0 decay point producing too slow trajectories (See **Figure S7**). After computing the CASSCF trajectories, in order to account the effect of dynamic electron correlation, the energy profiles of trajectories are recomputed using the CASPT2 level of theory with the standard three-root state average.

S2 Charge distribution on the rPSB11 chromophore

During the photoexcitation, rPSB11 undergoes a partial charge transfer of its positive charge from the $-C_{15}=N-$ side (the Schiff base moiety) to the σ skeleton side of the molecule.[63] The electronic character (charge transfer or biradical character) of each excited state, could be explored by looking at the charge distribution on a certain moiety of the molecule on corresponding excited state and compare it with the ground state charge distribution. For this aim, the charge distribution of the first four states of the representative model (model-6) are computed as the sum of the charges of all the atoms in the positive moiety (**Scheme S1**, $-^{+}H_2N=C_{15}-C_{14}=C_{13}-C_{12}$). The charge distribution of the first four roots of the rPSB11 in the representative model (model-6) with 8-root SA (used for calculating the TPA properties) and cc-pVTZ basis set is reported in **Table S2**. Decreasing the charge distribution of the positive moiety of S_1 state respect to S_0 state implies the charge transfer character of the S_1 excited state in agreement with previous studies. [63-65] However, the charge distribution of the S_2 and S_3 are not in agreement to the previous studies. For further exploration, the charge distribution is calculated for the representative model (model-6) with 3-root, 4-root and 5-root SA and cc-pVTZ basis set (**Table S2**). The charge distribution with 3-root SA reveals the charge transfer character of S_1 and biradical character of S_2 in agreement with previous reports.[63, 65] Consequently, as the number of roots in SA increases, the charge distribution of the S_2 and S_3 decreases which may attribute to the SA effect.

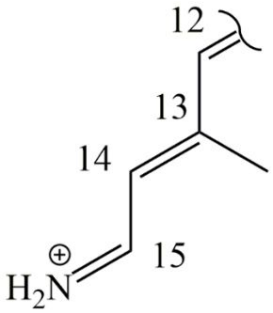

Scheme S1. *Positive moiety of rPSB11 which used to calculate the charge distribution (Table s2).*

Table. S2. *Distribution of positive charge on the displayed moiety (Scheme S3) of rPSB11 chromophore in the ground and first three excited states of the representative model (model-6) of Rh. Our 3-root SA results*

are in good agreement with the previous results.[63, 65] The decreasing of the S_2 charge with the increasing of the roots in state averaging (SA), is attributed to the SA effect.

	S_0	S_1	S_2	S_3
3-root SA	0.84	0.47	0.79	-
4-root SA	0.84	0.49	0.74	0.80
5-root SA	0.84	0.48	0.70	0.77
8-root SA	0.85	0.47	0.54	0.60

S3. OPA properties of the 10 independent Rh models

Table S3. *OPA excitation energies ($\Delta E_{S1\text{-}S0}$ and $\Delta E_{S2\text{-}S0}$), maximum absorption wavelengths (λ_{max}, nm), and oscillator strength (f_{Osc}) of the Rh models calculated at XMCQDPT2/cc-pVTZ//CASSCF/6-31G(d)/AMBER level of theory. Differences between calculated and experimental data ($\Delta\Delta E^{exp}_{S1\text{-}S0}$, $\Delta\lambda^{Exp}_{max}$) are also presented.*

	$S_0 \rightarrow S_1$					$S_0 \rightarrow S_2$				
Structure (seed)	$\Delta E_{S1\text{-}S0}$	λ_{max}	f_{Osc}	$\Delta\Delta E^{Exp}_{S1\text{-}S0}$	$\Delta\lambda^{Exp}_{max}$	$\Delta E_{S2\text{-}S0}$	λ_{max}	f_{Osc}	$\Delta\Delta E^{Exp}_{S2\text{-}S0}$	$\Delta\lambda^{Exp}_{max}$
	kcal/mol	**nm**		**kcal/mol**	**nm**	**kcal/mol**	**nm**		**kcal/mol**	**nm**
model 1 (1837)	61.0	469	0.86	3.6	−29	84.8	337	0.17	0.7	−3
model 2 (18273)	60.4	473	0.87	3.0	−25	84.8	337	0.19	0.7	−3
model 3 (28374)	59.8	478	0.87	2.4	−20	84.3	339	0.23	0.2	−1
model 4 (3824)	60.1	476	0.87	2.7	−22	83.6	342	0.17	−0.5	2
model 5 (4567)	59.7	479	0.89	2.3	−19	84.1	340	0.21	0.0	0.0
model 6 (55555)	60.2	475	0.87	2.8	−23	84.3	339	0.20	0.2	−1
model 7 (666)	59.8	478	0.88	2.4	−20	84.1	340	0.21	0.0	0.0
model 8 (7834)	59.8	478	0.88	2.4	−20	83.8	341	0.18	−0.3	1
model 9 (87657)	59.8	478	0.89	2.4	−20	84.1	340	0.21	0.0	0.0
model 10 (999)	61.0	469	0.88	3.6	−29	85.1	336	0.18	1.0	−4
Average	**60.1**	**475**		2.7	−23	84.3	339		0.2	−1.1
DESV.ST	**0.5**	**4**				**0.4**	**2**			
Exp	**57.4**	**498**				**84.1**	**340**			

S4. Accuracy of the XMCQDPT2 Method

In order to further assess the accuracy of the XMCQDPT2 method, the energy gap of the first two transitions (*i.e.* $S_0 \rightarrow S_1$ and $S_0 \rightarrow S_2$) were calculated and compared to the gaps obtained via a 3-root-state-average CASPT2 calculations (a commonly employed, single state multi-configurational second order perturbation theory method) and with the experimental values. As mentioned in subsection ***S1.2***, these calculations have been performed using the QM/MM model-6, taken as the representative of 10 QM/MM model replicas. **Table 1** summarizes the comparison between the OPA of different protocols and experimental values. It can be seen that the CASPT2 and XMCQDPT2 corrections on top of the CASSCF energies give results close to the experimental λ_{max} of the first (498 nm)[66] and second (340 nm)[67-70] transitions. More specifically, the obtained $S_0 \rightarrow S_1$ and $S_0 \rightarrow S_2$ excitation energies computed at the XMCQDPT2/cc-pVTZ//CASSCF/6-31G(d)/AMBER level are blue-shifted with respect to the value obtained with the CASPT2//CASSCF/6-31G(d)/AMBER values (see **Table S1**) when calculated with 3-root-state-average with 6-31G(d) basis set. The fact that the CASPT2 calculation yields transition energies closer to the experimental observed value, does not necessarily reflect a higher accuracy of the model but a different balance between errors of different sign as detailed in ref [17]. Additionally, we should note that the more advanced XMCQDPT2 method, being a multi-state method, accounts for state (*i.e.* root) mixing between the excited states included in the averaging, and it is, in principle, more accurate than the single-state CASPT2 method.

The effect of the basis set was also tested, and the results showed that the predicted 6-31G(d) OPA transition energies are more blue-shifted from experimental values. The best agreement between the computed and experimental transition energies is achieved with the cc-pVTZ basis set indicating that a correlation consistent basis set is a more acceptable choice for computing the spectroscopic parameters using a QM/MM models of Rh. Variation in the number of contributing roots in the state averaging from 3 to 8 roots, does not yield remarkable changes in the computed transition energies. Nevertheless, as mentioned in section ***S1.3***, a precise description of S_0, S_1, S_2 and S_3 requires the choice of eight lowest CASSCF roots.

S5. Accuracy of the QM/MM model

In a recent action spectroscopy experiment,[71] the UV-Vis absorption of rPSB11 is measured in the gas-phase and the position and strengths of the transitions to highly-excited electronic states are assigned using quantum mechanical calculations.[71] Such calculations resulted in the assignment of

the 68.9 kcal/mol (λ_{max} = 415 nm) and 80.5 kcal/mol (λ_{max} = 355 nm) transition energies to the $S_0 \rightarrow S_2$ and $S_0 \rightarrow S_3$ transitions of the chromophore with the same oscillator strength (*i.e.* 0.14). Both the $S_0 \rightarrow S_2$ and $S_0 \rightarrow S_3$ transitions in our QM/MM model are blue-shifted respect to the reported values (**Table 1** and **Table S3**) possibly due to the interaction of the chromophore with protein cavity. The peak separation (*i.e.* $\langle \Delta E_{S3-S2} \rangle$) computed using our XMCQDPT2/cc-pVTZ//CASSCF/6-31G(d)/AMBER Rh models is only 4.5 kcal/mol and therefore smaller than the reported 11.6 kcal/mol.[71] To investigate the effect of protein cavity on these transitions, we computed the OPA of the isolated chromophore keeping the same geometry that it has in Rh (**Table S4**).

Table. S4. *Excitation energies ($\Delta E_{S1\text{-}S0}$, kcal/mol) and maximum absorption wavelengths (λ_{max}, nm), and oscillator strength (f_{Osc}) of the isolated rPSB11 calculated at the XMCQDPT2/cc-pVTZ//CASSCF/6-31G(d) level of theory.*

	Franck-Condon excitation			*Oscillator Strength*		
Structure (seed)	$S_0 \rightarrow S_1$	$S_0 \rightarrow S_2$	$S_0 \rightarrow S_3$	$S_0 \rightarrow S_1$	$S_0 \rightarrow S_2$	$S_0 \rightarrow S_3$
model 1 (01837)	57.0 (501 nm)	79.4 (360 nm)	90.2 (317 nm)	0.91	0.21	
model 2 (18273)	56.5 (506 nm)	79.4 (360 nm)	89.1 (321 nm)	0.93	0.20	
model 3 (28374)	55.3 (517 nm)	79.6 (359 nm)	88.2 (324 nm)	0.94	0.22	
model 4 (3824)	55.9 (511 nm)	76.4 (374 nm)	88.2 (324 nm)	0.93	0.24	
model 5 (4567)	55.4 (516 nm)	79.4 (360 nm)	88.5 (323 nm)	0.96	0.22	0.17
model 6 (55555)	55.8 (512 nm)	79.4 (360 nm)	89.1 (321 nm)	0.95	0.22	0.17
model 7 (666)	55.6 (515 nm)	79.4 (360 nm)	88.8 (322 nm)	0.96	0.22	
model 8 (7834)	56.4 (507 nm)	79.4 (360 nm)	89.1 (321 nm)	0.95	0.20	
model 9 (87654)	55.6 (514 nm)	79.4 (360 nm)	88.8 (322 nm)	0.96	0.22	
model 10 (999)	55.8 (512 nm)	76.6 (373 nm)	89.3 (320 nm)	0.88	0.26	
Average	**55.9 (511 nm)**	**79.4 (363 nm)**	**89.1 (321 nm)**			
DESV.ST	**0.5 (4.8)**					

The results show an increased peak separation of 9.7 kcal/mol in good agreement with the reported gas-phase transitions energies with the difference ascribed to the different state averaging and geometries used in the calculations. The result support the conclusion that the protein environment decreases the differences between the $S_0 \rightarrow S_2$ and $S_0 \rightarrow S_3$ excitation energies as well as their intensity

relative to the $S_0 \rightarrow S_1$ excitation energy. In fact, in contrast with the charge transfer character of S_1, the computed positive charge distribution on the chromophore shows that S_2 and S_3 states have diradical character (**Table S2**) consistently with the same and relatively small values of their oscillator strengths (**Table 1, Table S3**).

To illustrate the possible structural differences between the 10 QM/MM model replicas optimized at the CASSCF/6-31G(d)/AMBER level of theory, we have pictured the structure of their Lys-QM subsystem in **Figure S3**. As observed in this figure, the modest geometrical difference is consistent with the limited variation of the computed ΔE_{S1-S0} transition energies (**Table 1** and **Table S1**). Indeed, it is apparent that the Lys-QM structure differs mainly in the configuration of the methyl substituent at C13.

The results of the OPA studies support the idea that our QM/MM models could be suitable for the calculation of TPA spectra.

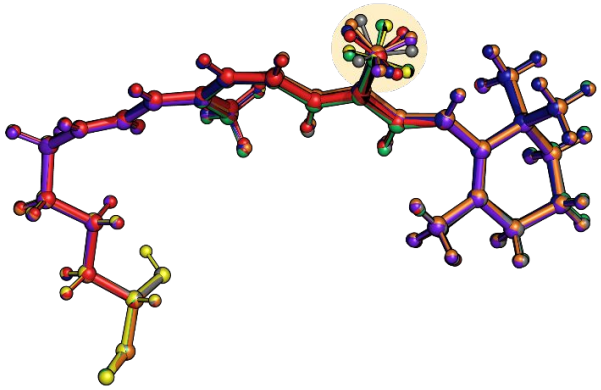

Figure S3*. Superposition of the Lys-QM subsystem of each of the 10 constructed Rh QM/MM models. The main structural differences are in the conformation of the methyl group bounded to carbon 13 of the rPSB11 chain.*

S6. TPA spectra of trans-stilbene and ACCD

The spectra of *trans*-stilbene and ACCD (their structures are shown in **Scheme S2**) calculated with the protocol described in the in the ***1.3*** section. The resultant spectra are shown in **Figure S4**.

Since the complete active space of the ACCD is too large to do CASSCF/6-31G(d) geometry optimization, the geometry of ACCD has optimized in the lower level of theory. However, before that we must be sure if this optimized geometry reproduces the TPA features of interested system similar to the CASSCF/6-31G(d) level of theory applied for *trans*-stilbene optimization. For this

reason, we used the optimized geometry of *trans*-stilbene at the MP2/ccpVTZ level of theory (which has been used in previous study[18]), to compute its TPA spectra with our protocol. The resultant geometry is very close to the optimized geometry at CASSCF/6-31G(d) level, and the TPA spectra is not intensely affected by the geometry as shown in **Figure S5**. Therefore, the geometry of ACCD is optimized at MP2/cc-pVTZ level of theory in this study and used for calculation of the TPA spectra.

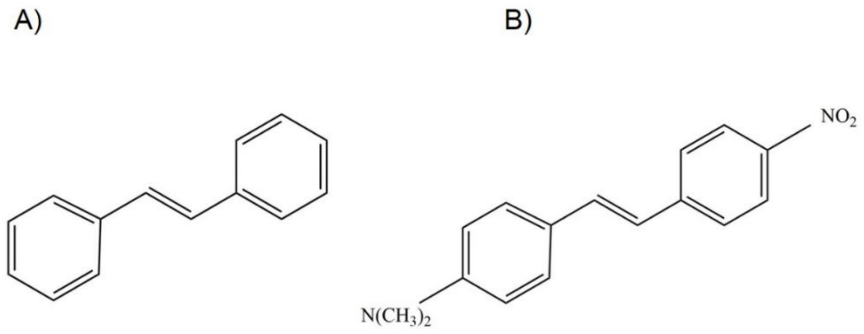

***Scheme S2**. Chemical structure of **A)** trans-stilbene and **B)** 4-Dimethylamino-4'-nitrostilbene (ACCD).*

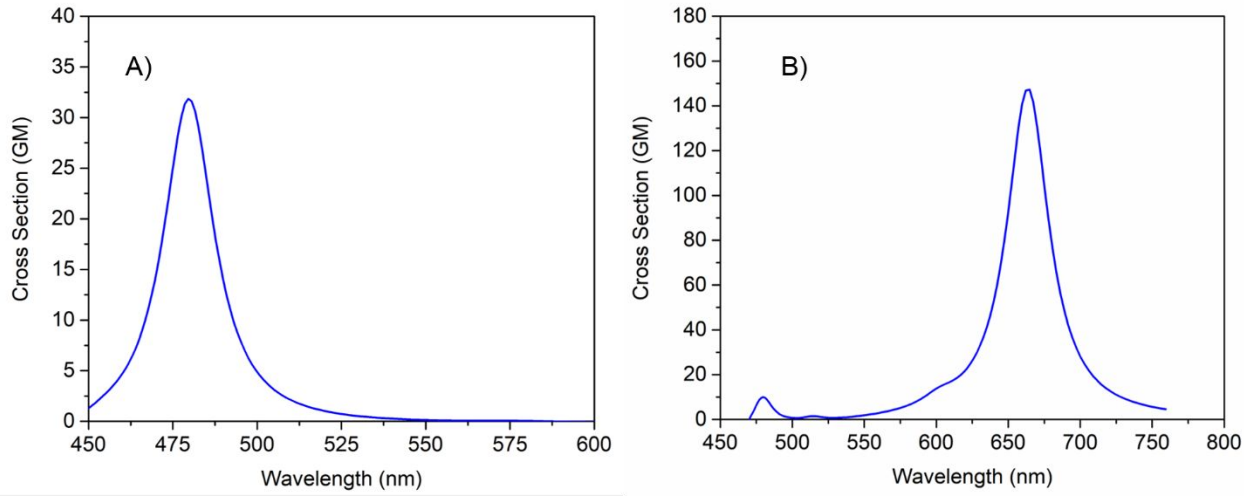

***Figure. S4. A)** TPA spectra of trans-stilbene and **B)** TPA spectra of 4-dimethylamino-4'-nitrostilbene (ACCD) in gas-phase in XMCQDPT2 level of theory with cc-pVTZ basis set.*

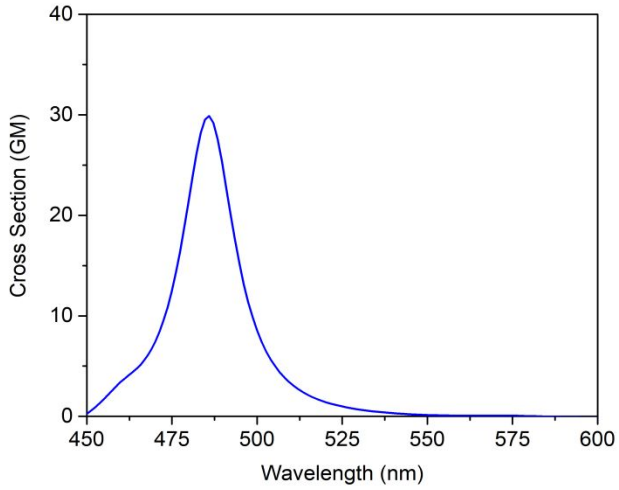

Figure. S5. *TPA spectra of trans-stilbene of MP2/cc-pVTZ optimized geometry calculated in the same level of theory of the Figure S4.*

Table S5. *Transition dipole moments (Debye), transition energies (nm) and oscillator strength of the OPA transitions for 12 states considered in SOS for trans-stilbene and ACCD. Here S_0 denotes the ground state and S_y is OPA excited state.*

	***trans*-stilbene**			**ACCD**		
$S_0 \rightarrow S_y$	$\langle S_0\|\mu\|S_y\rangle$ (*Debye*)	λ_{max} (*nm*)	f_{Osc}	$\langle S_0\|\mu\|S_y\rangle$ (*Debye*)	λ_{max} (*nm*)	f_{Osc}
$S_0 \rightarrow S_0$	0.0077			8.2277		
$S_0 \rightarrow S_1$	5.3787	292.19	0.47	7.8576	332.06	0.87
$S_0 \rightarrow S_2$	0.0667	287.92	0.00	0.6880	302.83	0.0073
$S_0 \rightarrow S_3$	4.9916	283.62	0.41	1.0407	301.05	0.017
$S_0 \rightarrow S_4$	0.1443	239.95	0.0004	2.0520	257.00	0.077
$S_0 \rightarrow S_5$	0.4625	227.80	0.0044	1.5146	248.58	0.043
$S_0 \rightarrow S_6$	0.2896	205.65	0.0019	1.6934	239.65	0.056
$S_0 \rightarrow S_7$	0.3453	194.85	0.0029	0.3657	217.56	0.0029
$S_0 \rightarrow S_8$	0.0230	194.45	0.00	0.4770	206.69	0.0052
$S_0 \rightarrow S_9$	0.0398	173.86	0.00	0.4957	201.30	0.0057
$S_0 \rightarrow S_{10}$	0.3903	170.07	0.0042	0.5933	180.09	0.0092
$S_0 \rightarrow S_{11}$	0.0138	157.08	0.00	0.3110	175.05	0.0026

S7. TPA properties of the isolated rPSB11

To calculate TPA properties (maximum absorption wavelength, $\lambda_{max,\,TPA}$ and cross-section, σ_{TPA}) of the isolated rPSB11, the same geometry of rPSB11 in Rh is taken in the absence of protein environment (in vacuum).

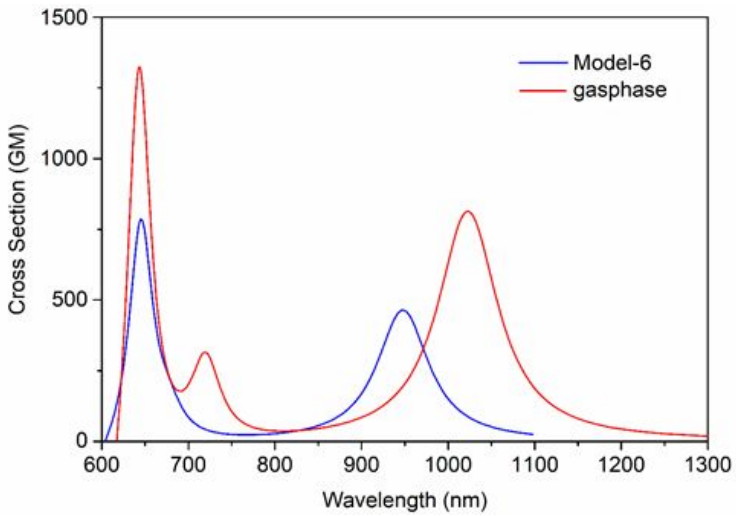

Figure. S6. *TPA spectra of rPSB11 in gas-phase (red) and in Rh protein environment (blue) in XMCQDPT2 level of theory with cc-pVTZ basis set. The simulated spectra reflect the common blue shift of the one-photon absorption spectra of Rh with respect to the chromophore in the gas-phase.*

S8. Orbital Character of the Two-photon transitions

As mentioned in the main text, TPA spectra of Rh show three intense peak corresponding to the $S_0 \rightarrow S_1$, $S_0 \rightarrow S_2$, and $S_0 \rightarrow S_3$ transitions. Here, we investigate the electronic nature of these two-photon transitions in terms of the transitions between the molecular orbitals. For this aim, we need to identify the intermediate states (reached by OPA) which their contribution to the SOS of the related TPA transitions is considerable. Looking at the transition dipole moment and dipole moment of the all possible transitions between the 12 selected roots reveals that the only three excited states *i.e.* S_1, S_2 and S_3 have the remarkable contribution to the SOS (based on the transition dipole moment of the excitation from ground state, Table S6) and therefore, could be considered as the intermediate states. For example, the important contributions to the SOS for $S_0 \rightarrow S_1$ TPA transition are: $S_0 \rightarrow S_1 \rightarrow S_1$, $S_0 \rightarrow S_2 \rightarrow S_1$ and $S_0 \rightarrow S_3 \rightarrow S_1$. Consequently, the wave function of those excited states was analyzed, and the most principal configurations of the excited states (with significant CI coefficient) were determined as shown in Table S7 and Figure S7. The results show the charge transfer character for $S_0 \rightarrow S_1$, $S_0 \rightarrow S_2$, and $S_0 \rightarrow S_3$ transitions, in agreement with the results of positive charge distribution on the chromophore (Table S2).

Table S6. *Transition dipole moments of essential intermediate OPA, and final TPA transitions contributing to the $S_0 \rightarrow S_1$, $S_0 \rightarrow S_2$, and $S_0 \rightarrow S_3$ two-photon transitions. Here S_0 denotes the ground state, S_y is OPA (intermediate) excited state and S_x is the final TPA excited state.*

Two-photon Transition **($S_0 \rightarrow S_x$)**	**$S_0 \rightarrow S_y \rightarrow S_x$**	**$\langle S_0\|\mu\|S_y\rangle$ (*Debye*)**	**$\langle S_y\|\mu\|S_x\rangle$ (*Debye*)**
$S_0 \rightarrow S_1$	$S_0 \rightarrow S_1 \rightarrow S_1$	9.4	15.0
	$S_0 \rightarrow S_2 \rightarrow S_1$	3.8	5.0
	$S_0 \rightarrow S_3 \rightarrow S_1$	3.8	7.5
$S_0 \rightarrow S_2$	$S_0 \rightarrow S_1 \rightarrow S_2$	9.4	5.0
	$S_0 \rightarrow S_2 \rightarrow S_2$	3.8	14.0
	$S_0 \rightarrow S_3 \rightarrow S_2$	3.8	7.0
$S_0 \rightarrow S_3$	$S_0 \rightarrow S_1 \rightarrow S_3$	9.4	7.5
	$S_0 \rightarrow S_2 \rightarrow S_3$	3.8	7.0
	$S_0 \rightarrow S_3 \rightarrow S_3$	3.8	12.6

Table S7. *Principal configurations of S_1, S_2 and S_3 electronic states involving in the $S_0 \rightarrow S_1$, $S_0 \rightarrow S_2$, and $S_0 \rightarrow S_3$ OPA (intermediate) transitions. Here H and L denote HOMO and LUMO, respectively.*

Electronic state	***Principal Configurations***	***weight***
S_1	$(H-1)^2H^1L^1(L+1)^0$ (α)	0.46
	$(H-1)^2H^1L^1(L+1)^0$ (β)	0.46
	$(H-1)^2H^1L^0(L+1)^1$ (α,β)*	0.31
	$(H-1)^2H^1L^0(L+1)^1$ (α)	0.26
	$(H-1)^2H^1L^0(L+1)^1$ (β)	0.26
S_2	$(H-1)^2H^1L^1(L+1)^0$ (α,β)*	0.44
	$(H-1)^2H^1L^1(L+1)^0$ (α)	0.32
	$(H-1)^2H^1L^1(L+1)^0$ (β)	0.32
	$(H-1)^1H^2L^1(L+1)^0$ (α)	0.24
	$(H-1)^1H^2L^1(L+1)^0$ (β)	0.24
S_3	$(H-1)^1H^2L^1(L+1)^0$ (α)	0.25
	$(H-1)^1H^2L^1(L+1)^0$ (β)	0.25
	$(H-1)^2H^1L^1(L+1)^0$ (α) + $(H-1)^1H^2L^1(L+1)^0$ (β)	0.25
	$(H-1)^1H^2L^1(L+1)^0$ (α) + $(H-1)^2H^1L^1(L+1)^0$ (β)	0.25

* Double excitation (both α and β electrons are excited simultaneously)

For the $S_0 \rightarrow S_1$ transition, based on the molecular orbitals (Figure S7), if we consider the five approximately parallel double bonds in the chain, the HOMO is bonding (or nearly so) with respect to the first four, and the LUMO is antibonding with respect to all five. This leads to the nice parallel

contributions to the overall transition dipole moment and hence, intense one-photon absorption. This one-photon transition has the main contribution to the $S_0 \rightarrow S_2$ and $S_0 \rightarrow S_3$ two-photon transitions (main text and Table S6) as an intermediate transition. As a result, these two transitions are not weak in TPA.

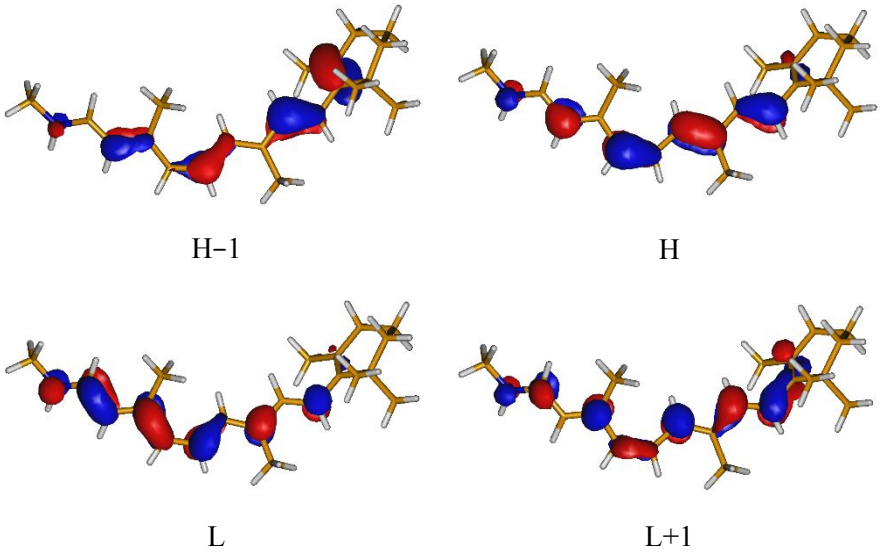

Figure S7. *Contributed molecular orbitals in the $S_0 \rightarrow S_1$, $S_0 \rightarrow S_2$, and $S_0 \rightarrow S_3$ transitions.*

S9. Energies, BLA, dihedrals and HOOP profiles along FC trajectories

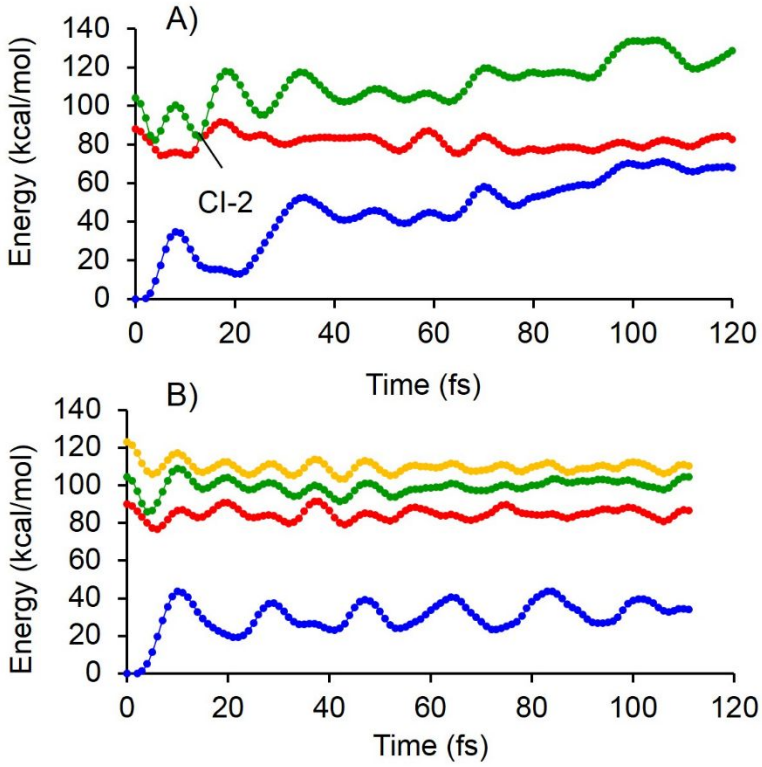

Figure S8. *Semi-classical trajectories of A) photoisomerization after population of the S_2 state with three-root state average and B) photoisomerization after population of the S_3 state with four-root state average at CASSCF level of theory. While a charge-transfer character dominates the S_1 state, the third and fourth roots (S_2 and S_3) have covalent (diradical) character leading to a far too high covalent character of the S_1 state upon state averaging. This leads to a S_1 gradient (i.e. slope of the S_1 potential energy surface), which is significantly lower than the correct one as the system progress towards the S_1 to S_0 decay point producing too slow trajectories.*

The geometrical progression of rPSB11 along the FC trajectories after populating the S_1, S_2 and S_3 has been shown in **Figure S9**. Here, we plotted dihedral angles (C_8–C_9=C_{10}–C_{11}, C_{10}–C_{11}=C_{12}–C_{13}, C_{14}–C_{15}=N–C_δ), hydrogen out-of-plane dihedral (HOOP), and bond length alteration (BLA, coordinate defined as the difference between the average single-bond length and the average double-bond length of the rPSB11 backbone) as a function of time. In the case of reactive S_1, S_2 populations (**Figure S9A** and **S9B**, respectively), the dihedral angle describing the isomerization of the C_{11}=C_{12} double bond (*i.e.* C_{10}–C_{11}=C_{12}–C_{13}) reaches the typical −90° value of a conical intersection (CI) at decay time (~100 fs). This reduction is compensated by increasing the adjacent C_8–C_9=C_{10}–C_{11}

dihedral. It is proposed that after populating the excited states, rPSB11 chromophore undergoes a vibrationally phased motion along critical modes such as BLA stretching and HOOP wagging[72] driving the population toward a CI. In both trajectories, an initially relaxation along BLA stretching mode is observed due to the unlocking the double bonds and locking the single bonds of rPSB11 (**Figure S9**). The unreactive S_3 population doesn't show the similar features of the reactive trajectories (**Figure S9C**). More details on the geometrical changes along the FC trajectories could be found in the literatures.[63, 72]

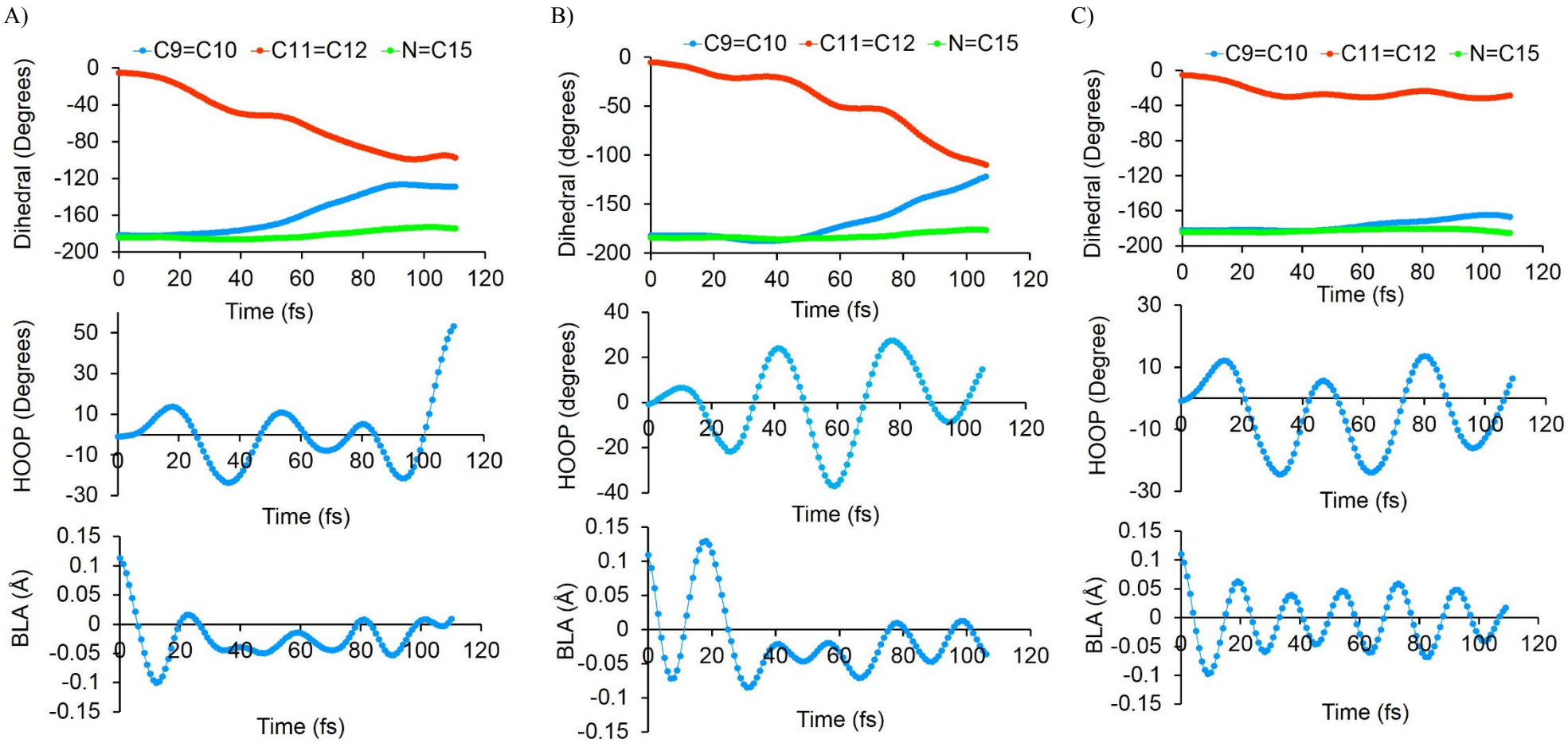

Figure S9. *Geometrical variation along the FC trajectories of A) Photoisomerization after population of the S_1 state. B) Photoisomerization after population of the S_2 state. C) Photoisomerization after population of the S_3 state.*

References:

1. Pedraza-González, L.; De Vico, L.; Marín, M. a. d. C.; Fanelli, F.; Olivucci, M. a-ARM: Automatic Rhodopsin Modeling with Chromophore Cavity Generation, Ionization State Selection, and External Counterion Placement. *J. Chem. Theory Comput.* **2019,** *15* (5), 3134-3152.
2. Melaccio, F.; del Carmen Marín, M.; Valentini, A.; Montisci, F.; Rinaldi, S.; Cherubini, M.; Yang, X.; Kato, Y.; Stenrup, M.; Orozco-Gonzalez, Y. Toward automatic rhodopsin modeling as a tool for high-throughput computational photobiology. *J. Chem. Theory Comput.* **2016,** *12* (12), 6020-6034.
3. Ferré, N.; Olivucci, M. Probing the rhodopsin cavity with reduced retinal models at the CASPT2//CASSCF/AMBER level of theory. *J. Am. Chem. Soc.* **2003,** *125* (23), 6868-6869.
4. Ferre, N.; Cembran, A.; Garavelli, M.; Olivucci, M. Complete-active-space self-consistent-field/Amber parameterization of the Lys296–retinal–Glu113 rhodopsin chromophore-counterion system. *Theor. Chem. Acc.* **2004,** *112* (4), 335-341.
5. Okada, T.; Sugihara, M.; Bondar, A.-N.; Elstner, M.; Entel, P.; Buss, V. The retinal conformation and its environment in rhodopsin in light of a new 2.2 Å crystal structure. *J. Mol. Biol.* **2004,** *342* (2), 571-583.
6. Zhang, L.; Hermans, J. Hydrophilicity of cavities in proteins. *Proteins: Struct., Funct., Bioinf.* **1996,** *24* (4), 433-438.
7. Pronk, S.; Páll, S.; Schulz, R.; Larsson, P.; Bjelkmar, P.; Apostolov, R.; Shirts, M. R.; Smith, J. C.; Kasson, P. M.; Van Der Spoel, D. GROMACS 4.5: a high-throughput and highly parallel open source molecular simulation toolkit. *Bioinformatics* **2013,** *29* (7), 845-854.
8. Aquilante, F.; Autschbach, J.; Carlson, R. K.; Chibotaru, L. F.; Delcey, M. G.; De Vico, L.; Fdez. Galván, I.; Ferré, N.; Frutos, L. M.; Gagliardi, L. Molcas 8: New capabilities for multiconfigurational quantum chemical calculations across the periodic table. *J. Comput. Chem.* **2016,** *37* (5), 506-541.
9. Rackers, J. A.; Wang, Z.; Lu, C.; Laury, M. L.; Lagardere, L.; Schnieders, M. J.; Piquemal, J.-P.; Ren, P.; Ponder, J. W. Tinker 8: software tools for molecular design. *J. Chem. Theory Comput.* **2018,** *14* (10), 5273-5289.
10. Cornell, W. D.; Cieplak, P.; Bayly, C. I.; Gould, I. R.; Merz, K. M.; Ferguson, D. M.; Spellmeyer, D. C.; Fox, T.; Caldwell, J. W.; Kollman, P. A. A second generation force field for the simulation of proteins, nucleic acids, and organic molecules. *J. Am. Chem. Soc.* **1995,** *117* (19), 5179-5197.
11. Ferré, N.; Ángyán, J. G. Approximate electrostatic interaction operator for QM/MM calculations. *Chem. Phys. Lett.* **2002,** *356* (3-4), 331-339.
12. Melaccio, F.; Olivucci, M.; Lindh, R.; Ferré, N. Unique QM/MM potential energy surface exploration using microiterations. *Int. J. Quantum Chem.* **2011,** *111* (13), 3339-3346.
13. Huntress, M. M.; Gozem, S.; Malley, K. R.; Jailaubekov, A. E.; Vasileiou, C.; Vengris, M.; Geiger, J. H.; Borhan, B.; Schapiro, I.; Larsen, D. S. Toward an understanding of the retinal chromophore in rhodopsin mimics. *J. Phys. Chem. B.* **2013,** *117* (35), 10053-10070.
14. Manathunga, M.; Yang, X.; Luk, H. L.; Gozem, S.; Frutos, L. M.; Valentini, A.; Ferrè, N.; Olivucci, M. Probing the photodynamics of rhodopsins with reduced retinal chromophores. *J. Chem. Theory Comput.* **2016,** *12* (2), 839-850.
15. Granovsky, A. A. F. v. h. c. c. m. s. g. f. i. h.
16. Granovsky, A. A. Extended multi-configuration quasi-degenerate perturbation theory: The new approach to multi-state multi-reference perturbation theory. *J. Chem. Phys.* **2011,** *134* (21), 214113.
17. Gozem, S.; Melaccio, F.; Lindh, R.; Krylov, A. I.; Granovsky, A. A.; Angeli, C.; Olivucci, M. Mapping the excited state potential energy surface of a retinal chromophore model with multireference and equation-of-motion coupled-cluster methods. *J. Chem. Theory Comput.* **2013,** *9* (10), 4495-4506.
18. Ioffe, I.; Granovsky, A. Photoisomerization of stilbene: The detailed XMCQDPT2 treatment. *J. Chem. Theory Comput.* **2013,** *9* (11), 4973-4990.
19. Goeppert-Mayer, M. M. Göppert-Mayer, Ann. Phys.(Leipzig) 9, 273 (1931). *Ann. Phys.(Leipzig)* **1931,** *9*, 273.
20. Kaiser, W.; Garrett, C. Two-photon excitation in Ca F 2: Eu 2+. *Phys. Rev. Lett.* **1961,** *7* (6), 229.

21. Filippidis, G.; Gualda, E.; Mari, M.; Troulinaki, K.; Fotakis, C.; Tavernarakis, N. In vivo imaging of cell morphology and cellular processes in Caenorhabditis elegans, using non-linear phenomena. *Micron* **2009,** *40* (8), 876-880.
22. SLYFIELD Jr, C. R.; Niemeyer, K. E.; Tkachenko, E. V.; TOMLINSON, R. E.; STEYER, G. G.; PATTHANACHAROENPHON, C. G.; KAZAKIA, G. J.; WILSON, D. L.; HERNANDEZ, C. J. Three-dimensional surface texture visualization of bone tissue through epifluorescence-based serial block face imaging. *J. Microsc.* **2009,** *236* (1), 52-59.
23. He, G. S.; Zheng, Q.; Prasad, P. N.; Grote, J. G.; Hopkins, F. K. Infrared two-photon-excited visible lasing from a DNA-surfactant-chromophore complex. *Opt. Lett.* **2006,** *31* (3), 359-361.
24. Bhawalkar, J.; He, G.; Prasad, P. Nonlinear multiphoton processes in organic and polymeric materials. *Rep. Prog. Phys.* **1996,** *59* (9), 1041.
25. Zhang, L.; Allen, S. D.; Woelfle, C.; Zhang, F. Influence of polymer structures on optical power limiting performance of single-walled carbon nanotubes. *J. Phys. Chem. C.* **2009,** *113* (31), 13979-13984.
26. Lemercier, G.; Bonne, A.; Four, M.; Lawson-Daku, L. M. 3MLCT excited states in Ru (II) complexes: Reactivity and related two-photon absorption applications in the near-infrared spectral range. *Comptes Rendus Chimie* **2008,** *11* (6-7), 709-715.
27. Li, X. Strain induced semiconductor nanotubes: from formation process to device applications. *J. Phys. D.* **2008,** *41* (19), 193001.
28. Juodkazis, S.; Mizeikis, V.; Matsuo, S.; Ueno, K.; Misawa, H. Three-dimensional micro-and nano-structuring of materials by tightly focused laser radiation. *Bull. Chem. Soc. Jpn.* **2008,** *81* (4), 411-448.
29. Zijlstra, P.; Chon, J. W.; Gu, M. Five-dimensional optical recording mediated by surface plasmons in gold nanorods. *Nature.* **2009,** *459* (7245), 410.
30. Tsuji, M.; Nishizawa, N.; Kawata, Y. Three-dimensional two-photon bit-recording with a compact fiber laser. *IEEE Trans. Magn.* **2009,** *45* (5), 2232-2235.
31. Mikhailov, I. A.; Belfield, K. D.; Masunov, A. E. DFT-based methods in the design of two-photon operated molecular switches. *J. Phys. Chem. A.* **2009,** *113* (25), 7080-7089.
32. Oron, D.; Papagiakoumou, E.; Anselmi, F.; Emiliani, V. Two-photon optogenetics. In *Prog. Brain. Res.*, Elsevier: 2012; Vol. 196, pp 119-143.
33. Denk, W.; Strickler, J. H.; Webb, W. W. Two-photon laser scanning fluorescence microscopy. *Science.* **1990,** *248* (4951), 73-76.
34. Rickgauer, J. P.; Tank, D. W. Two-photon excitation of channelrhodopsin-2 at saturation. *Proc. Natl. Acad. Sci.* **2009**, pnas. 0907084106.
35. Mohanty, S. K.; Reinscheid, R. K.; Liu, X.; Okamura, N.; Krasieva, T. B.; Berns, M. W. In-depth activation of channelrhodopsin 2-sensitized excitable cells with high spatial resolution using two-photon excitation with a near-infrared laser microbeam. *Biophys. J.* **2008,** *95* (8), 3916-3926.
36. Andrasfalvy, B. K.; Zemelman, B. V.; Tang, J.; Vaziri, A. Two-photon single-cell optogenetic control of neuronal activity by sculpted light. *Proc. Natl. Acad. Sci.* **2010,** *107* (26), 11981-11986.
37. Fenno, L.; Yizhar, O.; Deisseroth, K. The development and application of optogenetics. *Annu. Rev. Neurosci.* **2011,** *34*.
38. Papagiakoumou, E.; Anselmi, F.; Bègue, A.; De Sars, V.; Glückstad, J.; Isacoff, E. Y.; Emiliani, V. Scanless two-photon excitation of channelrhodopsin-2. *Nat. Methods.* **2010,** *7* (10), 848.
39. Deisseroth, K. Optogenetics: 10 years of microbial opsins in neuroscience. *Nat. Neurosci.* **2015,** *18* (9), 1213.
40. Prakash, R.; Yizhar, O.; Grewe, B.; Ramakrishnan, C.; Wang, N.; Goshen, I.; Packer, A. M.; Peterka, D. S.; Yuste, R.; Schnitzer, M. J. Two-photon optogenetic toolbox for fast inhibition, excitation and bistable modulation. *Nat. Methods.* **2012,** *9* (12), 1171.
41. Forli, A.; Vecchia, D.; Binini, N.; Succol, F.; Bovetti, S.; Moretti, C.; Nespoli, F.; Mahn, M.; Baker, C. A.; Bolton, M. M. Two-Photon Bidirectional Control and Imaging of Neuronal Excitability with High Spatial Resolution In Vivo. *Cell Rep.* **2018,** *22* (11), 3087-3098.

42. Chung, S.-J.; Zheng, S.; Odani, T.; Beverina, L.; Fu, J.; Padilha, L. A.; Biesso, A.; Hales, J. M.; Zhan, X.; Schmidt, K. Extended squaraine dyes with large two-photon absorption cross-sections. *J. Am. Chem. Soc.* **2006,** *128* (45), 14444-14445.
43. Williams-Harry, M.; Bhaskar, A.; Ramakrishna, G.; Goodson, T.; Imamura, M.; Mawatari, A.; Nakao, K.; Enozawa, H.; Nishinaga, T.; Iyoda, M. Giant thienylene-acetylene-ethylene macrocycles with large two-photon absorption cross section and semishape-persistence. *J. Am. Chem. Soc.* **2008,** *130* (11), 3252-3253.
44. Sun, C.-L.; Liao, Q.; Li, T.; Li, J.; Jiang, J.-Q.; Xu, Z.-Z.; Wang, X.-D.; Shen, R.; Bai, D.-C.; Wang, Q. Rational design of small indolic squaraine dyes with large two-photon absorption cross section. *Chem. Sci.* **2015,** *6* (1), 761-769.
45. Albota, M.; Beljonne, D.; Brédas, J.-L.; Ehrlich, J. E.; Fu, J.-Y.; Heikal, A. A.; Hess, S. E.; Kogej, T.; Levin, M. D.; Marder, S. R. Design of organic molecules with large two-photon absorption cross sections. *Science.* **1998,** *281* (5383), 1653-1656.
46. Beerepoot, M. T.; Friese, D. H.; List, N. H.; Kongsted, J.; Ruud, K. Benchmarking two-photon absorption cross sections: performance of CC2 and CAM-B3LYP. *Phys. Chem. Chem. Phys.* **2015,** *17* (29), 19306-19314.
47. Morel, Y.; Irimia, A.; Najechalski, P.; Kervella, Y.; Stephan, O.; Baldeck, P. L.; Andraud, C. Two-photon absorption and optical power limiting of bifluorene molecule. *J. Chem. Phys.* **2001,** *114* (12), 5391-5396.
48. Nayyar, I. H.; Masunov, A. m. E.; Tretiak, S. Comparison of TD-DFT methods for the calculation of two-photon absorption spectra of oligophenylvinylenes. *J. Phys. Chem. C.* **2013,** *117* (35), 18170-18189.
49. Fortrie, R.; Chermette, H. Two-photon absorption strength: A new tool for the quantification of two-photon absorption. *J. Chem. Phys.* **2006,** *124* (20), 204104.
50. Hu, Z.; Wang, W.; Khadka, V. S.; Galipeau, D. W.; Yan, X. Quantum mechanical modelling and calculation of two-photon absorption properties of new class 'Λ'-shaped conjugated molecules. *Mol. Simulat.* **2011,** *37* (06), 431-439.
51. Sneskov, K.; Olsen, J. M. H.; Schwabe, T.; Hättig, C.; Christiansen, O.; Kongsted, J. Computational screening of one-and two-photon spectrally tuned channelrhodopsin mutants. *Phys. Chem. Chem. Phys.* **2013,** *15* (20), 7567-7576.
52. De Wergifosse, M.; Houk, A. L.; Krylov, A. I.; Elles, C. G. Two-photon absorption spectroscopy of trans-stilbene, cis-stilbene, and phenanthrene: Theory and experiment. *J. Chem. Phys.* **2017,** *146* (14), 144305.
53. Drobizhev, M.; Makarov, N. S.; Tillo, S. E.; Hughes, T. E.; Rebane, A. Two-photon absorption properties of fluorescent proteins. *Nat. Methods.* **2011,** *8* (5), 393.
54. Paterson, M. J.; Christiansen, O.; Pawłowski, F.; Jørgensen, P.; Hättig, C.; Helgaker, T.; Sałek, P. Benchmarking two-photon absorption with CC3 quadratic response theory, and comparison with density-functional response theory. *J. Chem. Phys.* **2006,** *124* (5), 054322.
55. Nanda, K. D.; Krylov, A. I. Two-photon absorption cross sections within equation-of-motion coupled-cluster formalism using resolution-of-the-identity and Cholesky decomposition representations: Theory, implementation, and benchmarks. *J. Chem. Phys.* **2015,** *142* (6), 064118.
56. Kuzyk, M. G.; Dirk, C. W. *Characterization techniques and tabulations for organic nonlinear optical materials*. Marcel Dekker: 1998.
57. Karotki, A. Simultaneous two-photon absorption of tetrapyrrolic molecules: from femtosecond coherence experiments to photodynamic therapy. Montana State University-Bozeman, College of Letters & Science, 2003.
58. Levenson, M. *Introduction to Nonlinear Laser Spectroscopy 2e*. Elsevier: 2012.
59. Orr, B.; Ward, J. Perturbation theory of the non-linear optical polarization of an isolated system. *Mol. Phys.* **1971,** *20* (3), 513-526.
60. Schapiro, I.; Ryazantsev, M. N.; Frutos, L. M.; Ferré, N.; Lindh, R.; Olivucci, M. The ultrafast photoisomerizations of rhodopsin and bathorhodopsin are modulated by bond length alternation and HOOP driven electronic effects. *J. Am. Chem. Soc.* **2011,** *133* (10), 3354-3364.

61. Hammes-Schiffer, S.; Tully, J. C. Proton transfer in solution: Molecular dynamics with quantum transitions. *J. Chem. Phys.* **1994,** *101* (6), 4657-4667.
62. Manathunga, M.; Yang, X.; Olivucci, M. Electronic State Mixing Controls the Photoreactivity of a Rhodopsin with all-trans Chromophore Analogues. *J. Phys. Chem. Lett.* **2018,** *9* (21), 6350-6355.
63. Manathunga, M.; Yang, X.; Orozco-Gonzalez, Y.; Olivucci, M. Impact of Electronic State Mixing on the Photoisomerization Time Scale of the Retinal Chromophore. *J. Phys. Chem. Lett.* **2017,** *8* (20), 5222-5227.
64. Cembran, A.; Bernardi, F.; Olivucci, M.; Garavelli, M. The retinal chromophore/chloride ion pair: Structure of the photoisomerization path and interplay of charge transfer and covalent states. *Proc. Natl. Acad. Sci.* **2005,** *102* (18), 6255-6260.
65. Frutos, L. M.; Andruniów, T.; Santoro, F.; Ferré, N.; Olivucci, M. Tracking the excited-state time evolution of the visual pigment with multiconfigurational quantum chemistry. *Proc. Natl. Acad. Sci.* **2007,** *104* (19), 7764-7769.
66. Morrow, J. M.; Castiglione, G. M.; Dungan, S. Z.; Tang, P. L.; Bhattacharyya, N.; Hauser, F. E.; Chang, B. S. An experimental comparison of human and bovine rhodopsin provides insight into the molecular basis of retinal disease. *FEBS Lett.* **2017,** *591* (12), 1720-1731.
67. Shichi, H. Biochemistry of visual pigments II. Phospholipid requirement and opsin conformation for regeneration of bovine rhodopsin. *J. Biol. Chem.* **1971,** *246* (20), 6178-6182.
68. Rafferty, C. N.; Cassim, J. Y.; McConnell, D. G. Circular dichroism, optical rotatory dispersion, and absorption studies on the conformation of bovine rhodopsin in situ and solubilized with detergent. *Biophysics of structure and mechanism* **1977,** *2* (4), 277-320.
69. Ebrey, T. G.; Honig, B. Ultraviolet chromophore transitions in the rhodopsin spectrum. *Proc. Natl. Acad. Sci.* **1972,** *69* (7), 1897-1899.
70. Crouch, R.; Purvin, V.; Nakanishi, K.; Ebrey, T. Isorhodopsin II: artificial photosensitive pigment formed from 9, 13-dicis retinal. *Proc. Natl. Acad. Sci.* **1975,** *72* (4), 1538-1542.
71. Knudsen, J. L.; Kluge, A.; Bochenkova, A. V.; Kiefer, H. V.; Andersen, L. H. The UV-visible action-absorption spectrum of all-trans and 11-cis protonated Schiff base retinal in the gas phase. *Phys. Chem. Chem. Phys.* **2018,** *20* (10), 7190-7194.
72. Gozem, S.; Luk, H. L.; Schapiro, I.; Olivucci, M. Theory and simulation of the ultrafast double-bond isomerization of biological chromophores. *Chem. Rev.* **2017,** *117* (22), 13502-13565.